

# Using Exciton/Trion Dynamics to Spatially Monitor the Catalytic Activities of MoS<sub>2</sub> during the Hydrogen Evolution Reaction

Fu-He Hsiao,<sup>†</sup> Cheng-Chu Chung,<sup>†</sup> Chun-Hao Chiang,<sup>†</sup> Wei-Neng Feng, Wen-Yen Tzeng, Hung-Min Lin, Chien-Ming Tu, Heng-Liang Wu, Yu-Han Wang, Wei-Yen Woon, Hsiao-Chien Chen, Ching-Hsiang Chen, Chao-Yuan Lo, Man-Hong Lai, Yu-Ming Chang, Li-Syuan Lu, Wen-Hao Chang, Chun-Wei Chen,\* and Chih-Wei Luo\*



Cite This: ACS Nano 2022, 16, 4298–4307



Read Online

ACCESS |

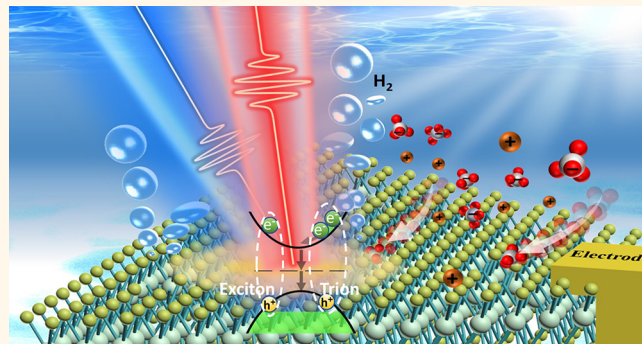
Metrics & More

Article Recommendations

Supporting Information

**ABSTRACT:** The adsorption and desorption of electrolyte ions strongly modulates the carrier density or carrier type on the surface of monolayer-MoS<sub>2</sub> catalyst during the hydrogen evolution reaction (HER). The buildup of electrolyte ions onto the surface of monolayer MoS<sub>2</sub> during the HER may also result in the formation of excitons and trions, similar to those observed in gate-controlled field-effect transistor devices. Using the distinct carrier relaxation dynamics of excitons and trions of monolayer MoS<sub>2</sub> as sensitive descriptors, an *in situ* microcell-based scanning time-resolved liquid cell microscope is set up to simultaneously measure the bias-dependent exciton/trion dynamics and spatially map the catalytic activity of monolayer MoS<sub>2</sub> during the HER. This operando probing technique used to monitor the interplay between exciton/trion dynamics and electrocatalytic activity for two-dimensional transition metal dichalcogenides provides an excellent platform to investigate the local carrier behaviors at the atomic layer/liquid electrolyte interfaces during electrocatalytic reaction.

**KEYWORDS:** hydrogen evolution reaction (HER), monolayer MoS<sub>2</sub>, exciton dynamics, trion dynamics, time-resolved microscopy



## INTRODUCTION

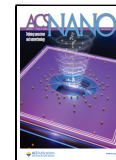
Hydrogen (H<sub>2</sub>) production by electrochemical and photoelectrochemical water splitting has become a promising sustainable energy source as an environmentally friendly technology for renewable energy.<sup>1</sup> An effective catalyst that facilitates charge transfer and reduces the overpotential is usually required for effective H<sub>2</sub> production. Although noble metal catalysts such as platinum (Pt) demonstrate the most effective catalytic activities for the hydrogen evolution reaction (HER) due to their low free energy of hydrogen absorption ( $\Delta G_H$ ),<sup>2,3</sup> the high price and scarcity of these materials could largely limit the scalability for H<sub>2</sub> production. Recently, two-dimensional (2D) transition metal dichalcogenides (TMDs),<sup>4,5</sup> such as MoS<sub>2</sub>, have emerged as a class of promising ultrathin catalysts for the HER, which exhibits great potential as an ideal replacement for noble metal electrocatalysts.<sup>6,7</sup> Extensive research has been focused on morphology designing, doping, and phase transitioning of 2D TMDs to enhance their electrocatalytic activities for the HER.<sup>8–13</sup> Recently, a self-

gating (or electrolyte-gating) phenomenon has been proposed to explain the excellent catalytic activity of ultrathin semiconductors such as 2D TMDs<sup>14</sup> although semiconductors have been considered as nonideal catalysts because they have a low concentration of intrinsic carriers.<sup>15</sup> The surface carrier concentrations for 2D TMD semiconductor catalysts are strongly modulated by electrolyte gating during electrocatalytic reactions, where n-type semiconductor catalysts usually favor cathodic reactions, such as the hydrogen evolution reaction, and p-type semiconductor catalysts prefer anodic reactions, such as the oxygen evolution reaction.<sup>14</sup> 2D TMD semi-

Received: November 23, 2021

Accepted: March 1, 2022

Published: March 7, 2022



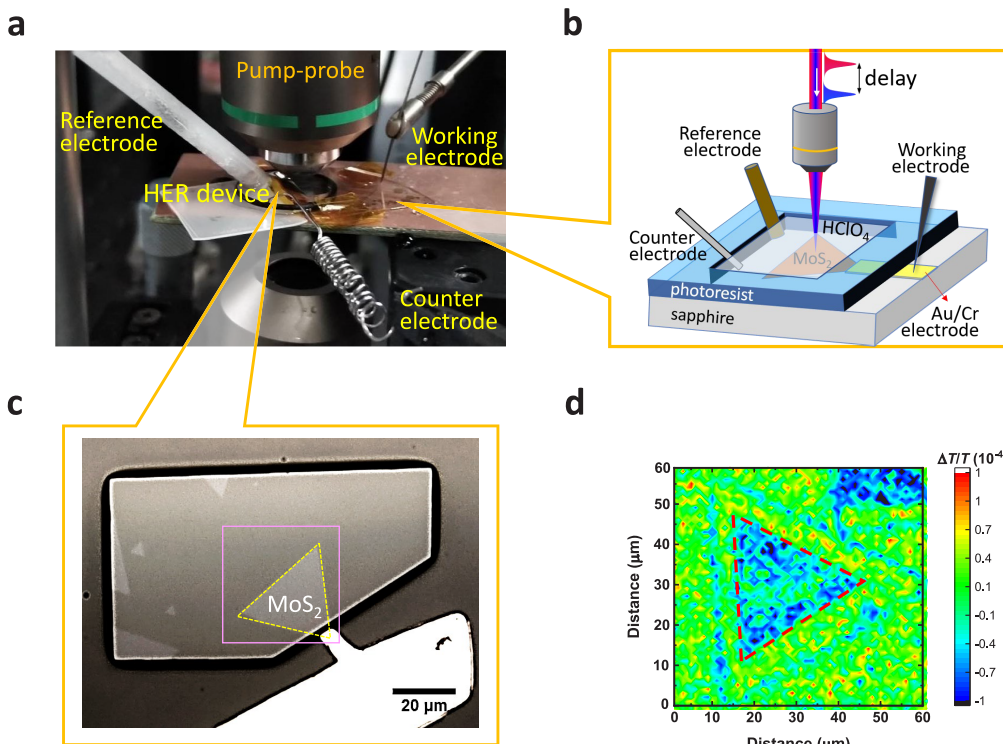


**Figure 1.** ML-MoS<sub>2</sub> hydrogen evolution reaction (HER) devices and the time-resolved liquid cell microscope (TR-LCM) for in situ probing ultrafast carrier dynamics. (a) Photos and (b) schematics of the HER device structure and the TR-LCM system for in situ probing ultrafast carrier dynamics at the ML MoS<sub>2</sub>/liquid electrolyte interface for the HER. (c) Photos of the HER device fabricated with a single ML-MoS<sub>2</sub> flake. The solid-pink square indicates the area for pump–probe measurements. (d) Typical pump–probe image at zero time delay ( $t = 0$  ps) with a TR-LCM.

conductor catalysts usually consist of a mixture of “active” (such as defects or edges) and “inert” sites,<sup>16</sup> and it is not fully understood how these sites are affected by electrolyte gating during electrocatalytic reactions. Therefore, it is important to investigate the spatially resolved catalytic activity at 2D TMD semiconductors due to self-gating (or electrolyte-gating) during electrocatalytic reactions to understand their fundamental mechanism of operation.

Because of the extremely large Coulomb interactions in atomically thin 2D materials, the formation of stable many-body bound states such as *excitons* (quasiparticles composed of an electron–hole pair) and negative *trions* (quasiparticles composed of two electrons and a hole) on monolayer (ML) MoS<sub>2</sub> at room temperature have been observed.<sup>17–20</sup> Excitons and trions exhibit distinct carrier dynamic behavior on ML MoS<sub>2</sub>, where excitons exhibit a longer nonradiative decay lifetime of several tens of picoseconds and trions have a much shorter lifetime of only a few picoseconds, due to electron transfer.<sup>21,22</sup> The formation of excitons and trions on ML MoS<sub>2</sub> strongly depends on the carrier density or carrier type, which can be controlled through several experimental approaches such as chemical doping, defect engineering, or control of gate voltage by field-effect transistor (FET) devices.<sup>23,24</sup> Additionally, the trions have been found to enhance the photocatalytic hydrogen evolution (PHE) efficiency in ReS<sub>2</sub> with monolayer-like structure.<sup>25</sup> A similar scenario may occur at the semiconductor/electrolyte interface of ML-MoS<sub>2</sub> catalyst during the HER process. The adsorption and desorption of hydrogen ions or electrolyte ions during HER may cause the strong modulation of carrier density or carrier type on the surface of ML-MoS<sub>2</sub> catalyst. Accordingly,

the electrolyte gating originating from the buildup of ions across the nanometer-scale electrochemical double layer (ECDL) may also result in the formation of excitons and trions at ML-MoS<sub>2</sub> catalyst.<sup>26</sup> Due to the distinct characteristic carrier dynamics of excitons and trions which are highly sensitive to the local charge environment affected by the adsorption and desorption of hydrogen ions or electrolyte ions, they can be used as the sensitive “descriptors” to in situ monitor the catalytic activity of MoS<sub>2</sub> during the HER.

In this work, through the setup of an in situ microcell-based scanning time-resolved liquid cell microscope (TR-LCM), we are able to simultaneously measure the bias-dependent exciton/trion dynamics and the catalytic activity of ML MoS<sub>2</sub> during the HER as shown in Figure 1. It is found that the individual percentages of excitons and trions on the surface of ML-MoS<sub>2</sub> catalyst can be modulated by electrolyte gating, which is strongly correlated with the electrocatalytic HER process. As the HER process is on, the surface of MoS<sub>2</sub> becomes “trion-dominant” while it becomes “exciton-dominant” as the HER process is off. The appearance or disappearance of excitons and trions on the surface of ML-MoS<sub>2</sub> catalyst strongly depends on the adsorption/desorption of hydrogen ions or electrolyte ions caused by electrolyte gating. Through 2D mapping images of the evolution of individual constituents of excitons and trions on the surface of ML MoS<sub>2</sub> during the HER process, the spatially resolved catalytic activity of ML MoS<sub>2</sub> affected by electrolyte gating can be unveiled. This platform not only allows us to explore the origin of the excellent catalytic activities of 2D TMD semiconductors due to the self-gating (or electrolyte-gating) effect but also provides us an operando technique to

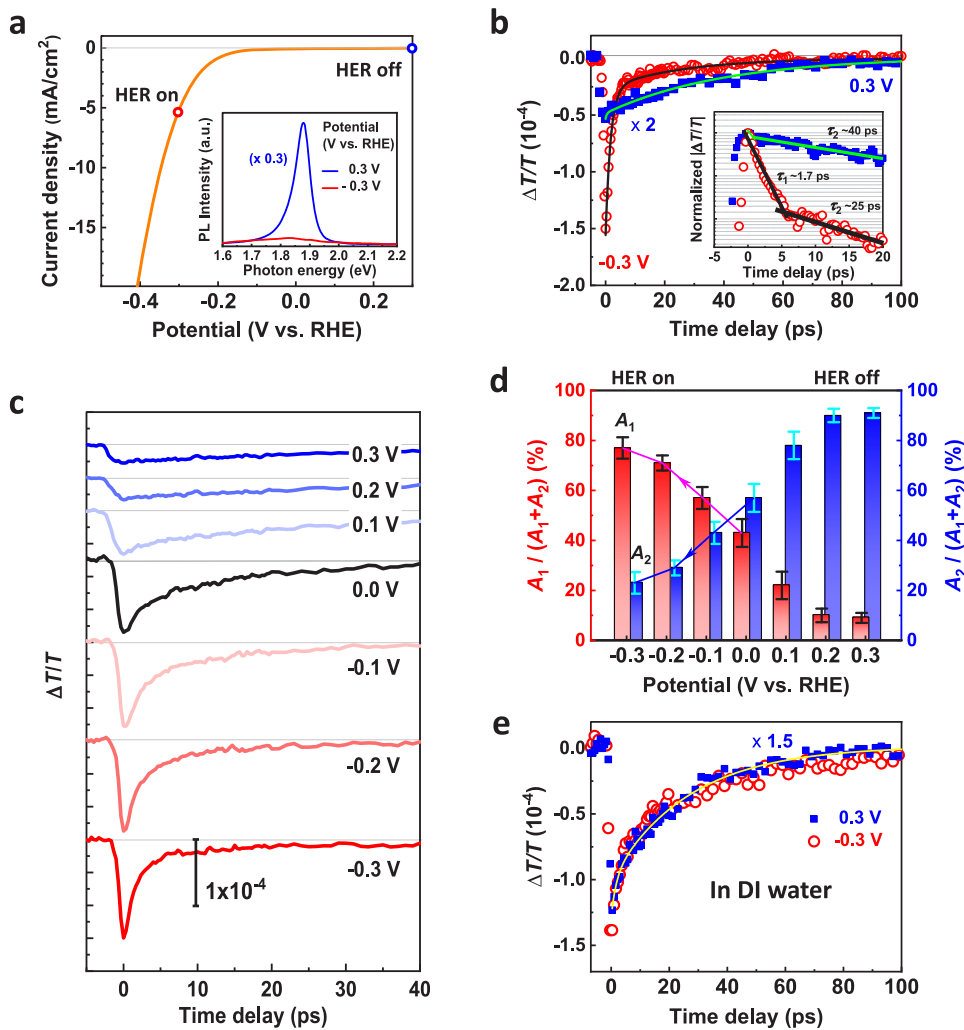


**Figure 2.** Potential-dependent ultrafast carrier dynamics for ML MoS<sub>2</sub> in a liquid electrolyte. (a) Current density as a function of potential for ML MoS<sub>2</sub> in HClO<sub>4</sub> electrolyte. Inset: PL spectra for ML MoS<sub>2</sub> in HClO<sub>4</sub> electrolyte with different potentials. (b) Typical pump–probe signals (transient transmittance changes,  $\Delta T/T$ ) of ML MoS<sub>2</sub> in HClO<sub>4</sub> electrolyte with different potentials (marked by open circles in part a). Inset: Normalized  $|\Delta T/T|$  of part b plotted in semilogarithmic scale. (c)  $\Delta T/T$  of ML MoS<sub>2</sub> in HClO<sub>4</sub> electrolyte with specific potentials (from 0.3 V to -0.3 V) in part a. (d) Amplitude ratio of the fast ( $A_1$ ) and slow ( $A_2$ ) relaxation components to the total amplitude ( $A_1 + A_2$ ) of  $\Delta T/T$  in part c with different potentials, respectively. (e) Typical  $\Delta T/T$  of ML MoS<sub>2</sub> in DI water with different potentials.

investigate the fundamental mechanism of 2D electrocatalysts during the electrochemical reaction.

## RESULTS AND DISCUSSION

**ML-MoS<sub>2</sub> HER Devices and TR-LCM for In Situ Probing Ultrafast Carrier Dynamics.** Figure 1a shows the photographic image of the in situ microcell-based scanning time-resolved liquid cell microscope (TR-LCM) which allows us to perform the simultaneous measurements of bias-dependent ultrafast carrier dynamics and electrochemical reactions at ML-MoS<sub>2</sub> catalyst during the HER process. A corresponding schematic setup is also shown in Figure 1b, where an ultrafast laser with  $400(\pm 8)/800(\pm 16)$  nm in wavelength and 100 fs in pulse width is used for the pump–probe measurements (typical pump and probe fluences are 200 and  $10 \mu\text{J}/\text{cm}^2$ , respectively) inside an electrolyte droplet with a spatial resolution of  $2 \mu\text{m}$ . Figure 1c shows the top view of an as-fabricated three-electrode ML-MoS<sub>2</sub> electrocatalytic device, for which a triangular single-crystal ML-MoS<sub>2</sub> flake with a typical grain size of  $\sim 40 \mu\text{m}$  was synthesized by chemical vapor deposition (CVD) and transferred to a quartz substrate. A Au/

Cr electrode was also deposited on one corner of a ML-MoS<sub>2</sub> flake, which allows us to provide the bias potential for the HER. The ML-MoS<sub>2</sub> device was then encapsulated by poly(methyl methacrylate) (PMMA) using the microcell-patterning technique (see Methods) so that only the area of a single-flake ML MoS<sub>2</sub> remained exposed for optical measurements. An electrolyte droplet (1 M HClO<sub>4</sub>, pH = 0.1) in which the reaction occurs was placed on top of the exposed ML-MoS<sub>2</sub> device. Further combining the TR-LCM with a scanner, we are able to obtain the 2D mapping image of ultrafast pump–probe signals (i.e., transient transmittance changes,  $\Delta T/T$ ) of ML MoS<sub>2</sub> in liquid electrolyte under different bias potentials during the HER as shown in Figure 1d.

**Potential-Dependent Ultrafast Carrier Dynamics for ML MoS<sub>2</sub> in a Liquid Electrolyte.** Figure 2a shows the linear sweep voltammogram (LSV) of a ML-MoS<sub>2</sub> electrochemical device during the HER using the fabricated microcell, where the onset potential of approximately -0.2 V versus the reversible hydrogen electrode (RHE) is obtained. As the bias potential  $V_{EC}$  is lower than -0.2 V vs RHE, the HER activity is significantly enhanced with increased current density, indicat-

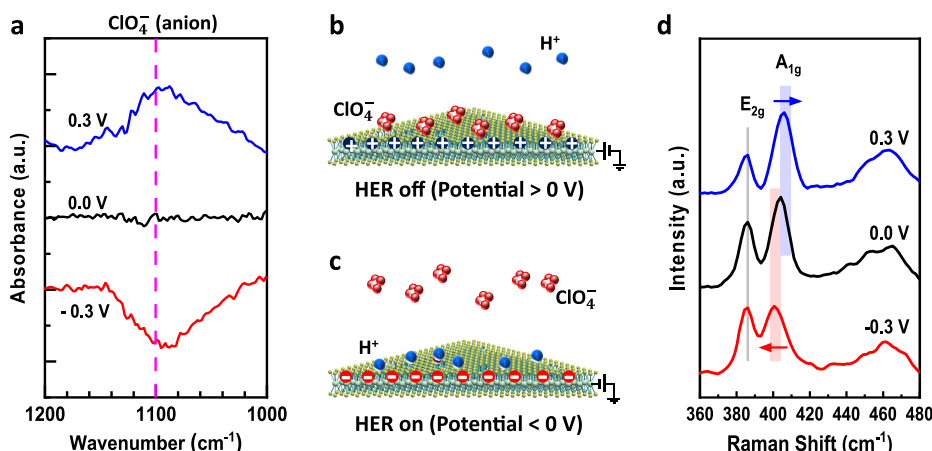


**Figure 3.** In situ IR absorbance/Raman spectra for ML MoS<sub>2</sub> in a liquid electrolyte. (a) IR differential absorbance for HClO<sub>4</sub> electrolyte in the ML-MoS<sub>2</sub> HER device with different electrochemical potentials. The reference condition is the ML-MoS<sub>2</sub> material in 1 M HClO<sub>4</sub> electrolyte at 0 V. For the details, please see the Methods. (b and c) Schematics of the microscopic mechanism for cations (H<sup>+</sup>) and anions (ClO<sub>4</sub><sup>-</sup>) on the surface of ML-MoS<sub>2</sub> HER devices at different electrochemical potentials. (d) Raman spectra for ML MoS<sub>2</sub> in HClO<sub>4</sub> electrolyte at different electrochemical potentials.

ing the HER process is “on”. By contrast, as the  $V_{EC}$  is greater than  $-0.1$  V vs RHE, the HER activity and current become negligible, indicating that the HER process is “off”. The inset of Figure 2a exhibits the representative photoluminescence (PL) spectra of an ML-MoS<sub>2</sub> electrochemical device under an applied electrochemical potential of  $V_{EC} = 0.3$  V and  $-0.3$  V vs RHE, corresponding to the HER-off and HER-on states, respectively. The PL spectrum at the HER-off state ( $V_{EC} = 0.3$  V vs RHE) features a stronger and sharper emission than that for the HER-on state ( $V_{EC} = -0.3$  V vs RHE). At the HER-off state, the strong PL spectrum with its peak position at the energy of  $1.88$  eV corresponds to exciton emission, while the PL spectrum at the HER-on state with its peak position that is red-shifted to a lower energy value of  $1.83$  eV corresponds to the trion emission of ML MoS<sub>2</sub>.<sup>17</sup> Similar results cannot be observed in an ML-MoS<sub>2</sub> electrochemical device with DI water. More detailed potential evolution and deconvoluted peak analysis of PL spectra can be found in Figure S1 of the Supporting Information.

The result indicates that the modulation of carrier density or carrier type on the surface of ML-MoS<sub>2</sub> catalyst by using different bias potentials during the HER process may result in the formation of excitons and trions, similar to those reports on ML MoS<sub>2</sub> by controlling the carrier density or carrier type through chemical doping or gate-voltage-controlled FET devices.<sup>23,24</sup> However, although the steady-state PL emission spectra at HER-off and HER-on states for ML-MoS<sub>2</sub> devices exhibit the typically optical signatures of excitons and trions at different electrolyte-gating conditions, the large spectral overlap between exciton and trion emissions and the significant suppression of the PL emission intensity mean that it is difficult to quantitatively differentiate the individual constituents of excitons and trions during the HER process (see the inset of Figure 2a). By contrast, Figure 2b exhibits the corresponding ultrafast carrier dynamics of a ML-MoS<sub>2</sub> electrochemical device at these two HER-off ( $V_{EC} = 0.3$  V vs RHE) and HER-on ( $V_{EC} = -0.3$  V vs RHE) states, where two distinct relaxation curves consisting of a fast relaxation component of  $\tau_1$  (<4 ps) with an amplitude of  $A_1$  and a slow component of  $\tau_2$  (16–40 ps) with an amplitude of  $A_2$  (see the inset of Figure 2b) can be deconvoluted and resolved. The

detailed results have been summarized in Figure S2 of the Supporting Information. At the HER-off state with  $V_{EC} = 0.3$  V vs RHE, the carrier dynamic relaxation curve is dominated by the slow component of  $\tau_2$ ; by contrast, the carrier dynamic behavior is dominated by the fast relaxation component of  $\tau_1$  when the  $V_{EC}$  is  $-0.3$  V vs RHE at the HER-on state. The individual constituents of  $(\tau_1, A_1)$  and  $(\tau_2, A_2)$  corresponding to the percentages of the respective contributions of excitons or trions can be obtained, which is consistent with the results of time-resolved PL in monolayer MoS<sub>2</sub>-based FET devices.<sup>27</sup> The quantitative information about the individual constituents of the well-resolved carrier dynamics for excitons and trions may thus act as the sensitive “descriptors” to account for the local environment due to the modulation of carrier density or carrier type on the ML-MoS<sub>2</sub> surface by electrolyte gating during the HER.

Figure 2c shows the evolution of the bias-dependent pump–probe signals ( $\Delta T/T$ ) of a ML-MoS<sub>2</sub> electrochemical device during the HER. The decay time for pump–probe signals changes significantly if  $V_{EC}$  changes from 0.3 to  $-0.3$  V vs RHE during the HER process, as measured by the TR-LCM. The individual fast and slow relaxation components of  $(\tau_1, A_1)$  and  $(\tau_2, A_2)$  for the measured bias-dependent  $\Delta T/T$  curves were further deconvoluted using the double-exponential decay function. Figure 2d shows the evolution of the percentages of individual components for  $(\tau_1, A_1)$  and  $(\tau_2, A_2)$  as a function of bias potential for the ML-MoS<sub>2</sub> catalyst during the HER process. At  $V_{EC} = 0.3$  V vs RHE (HER-off state), the measured pump–probe signals for ML MoS<sub>2</sub> are dominated by the slow component of  $(\tau_2, A_2)$  that results from the relaxation of excitons. The percentage ratio of  $A_2$  with respect to the total amplitude of  $A_1 + A_2$  (blue bars in Figure 2d) is about 90%. The percentage ratio of  $A_2$  decreases as the bias decreases from  $0.3$  V to  $-0.3$  V vs RHE. By contrast, the percentage of the fast component of  $(\tau_1, A_1)$  resulting from trions increases with decreasing the  $V_{EC}$  from  $0.3$  to  $-0.3$  V vs RHE. The percentage of  $A_1$  reaches a value of  $\sim 80\%$  at the potential of  $V_{EC} = -0.3$  V vs RHE, where the photoexcited carrier relaxation channel is dominated by the fast relaxation component of the trions as the ML-MoS<sub>2</sub> electrocatalytic device is at the HER-on state. The evolution of the percentage ratios of  $A_1$  and  $A_2$ , as

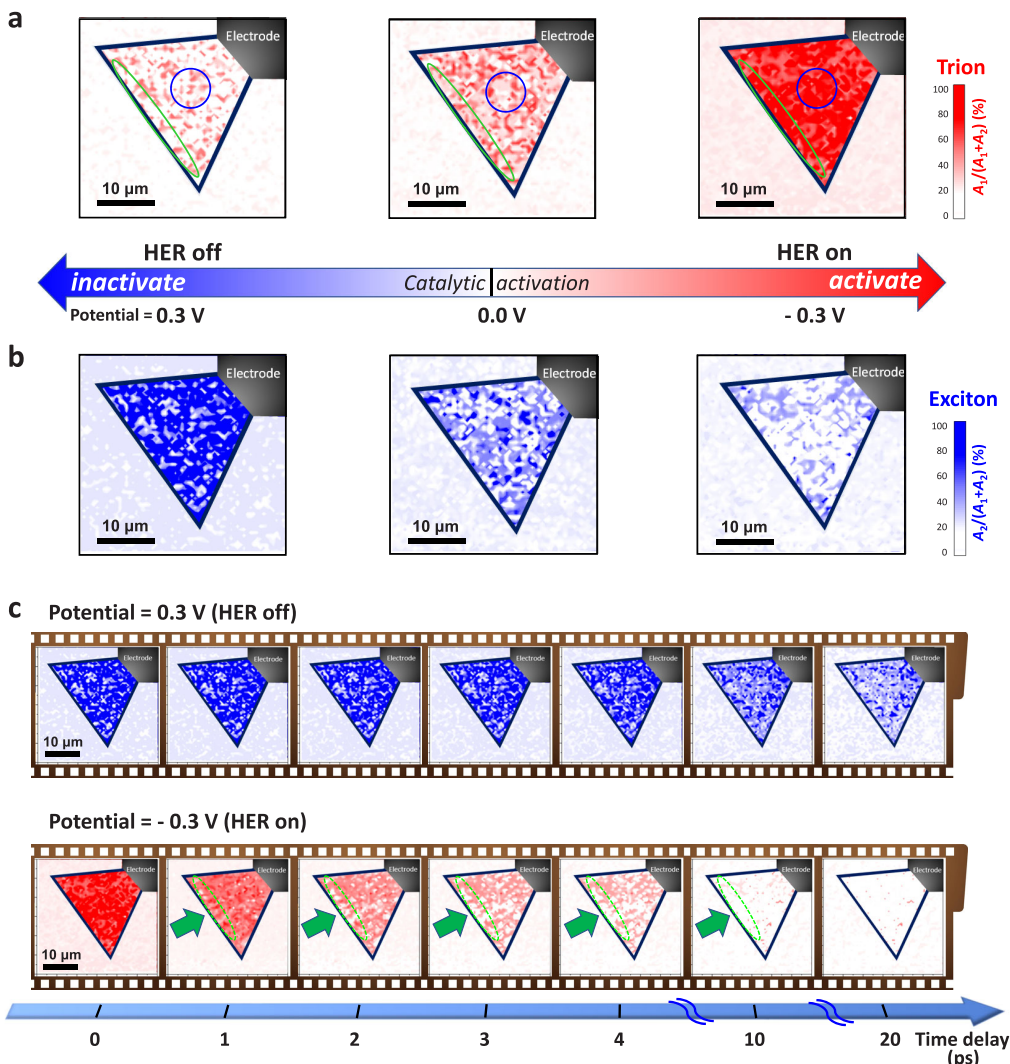


**Figure 4.** Ultrafast time evolution of trion and exciton distributions on ML MoS<sub>2</sub> in a liquid electrolyte. (a and b) Potential-dependent 2D mappings of the amplitude ratio for the fast ( $A_1$ ) and slow ( $A_2$ ) relaxation components to the total amplitude ( $A_1 + A_2$ ) of  $\Delta T/T$  in Figure 2d at zero time delay ( $t = 0$  ps) by the TR-LCM in Figure 1. Insets: a blue circle marks the measuring position for the basal region; a green ellipse marks the measuring position for the edge region. (c) Ultrafast time evolution of parts a and b. Trion (red) and exciton (blue) distributions on ML MoS<sub>2</sub> under liquid electrolyte HClO<sub>4</sub> at respective potentials of  $V_{EC} = -0.3$  and  $0.3$  V vs RHE. The green arrows and dashed ellipses indicate the inhomogeneous relaxation of trions.

obtained from the bias-dependent  $\Delta T/T$  curves using TR-LCM measurements, is significantly correlated with the catalytic activity of ML-MoS<sub>2</sub> electrochemical devices during the HER as shown in the LSV curve in Figure 2a. Figure 2e shows the bias-independent carrier dynamics for a ML-MoS<sub>2</sub> electrocatalytic device for which the electrolyte droplet of HClO<sub>4</sub> is replaced by deionized (DI) water at the potentials of  $V_{EC} = 0.3$  V and  $-0.3$  V vs RHE. There are no obvious changes in the measured pump–probe signals as seen above and in the in situ PL/Raman spectra, implying that the ionic electrolyte plays the key role for the observation of bias-dependent carrier dynamics in ML-MoS<sub>2</sub> electrocatalytic devices.

**In Situ IR Absorbance/Raman Spectra for ML MoS<sub>2</sub> in a Liquid Electrolyte.** To understand how electrolyte ions affect the observed bias-dependent carrier dynamics on the surface of ML-MoS<sub>2</sub> electrocatalyst devices, we have further performed in situ IR absorbance spectroscopy and in situ Raman spectroscopy measurements to monitor the modulation of the local charge redistribution on an ML-MoS<sub>2</sub> surface

affected by electrolyte gating during the HER. The detailed setups of the in situ IR and Raman spectroscopies are described in the Methods. Figure 3a shows the in situ IR absorption spectra, which exhibit a peak at  $1100\text{ cm}^{-1}$  as the bias potential varies from  $V_{EC} = 0.3$  V to  $-0.3$  V vs RHE. The intensity of the IR absorption spectrum of ML MoS<sub>2</sub> at  $V_{EC} = 0$  V vs RHE is the reference. An increase or decrease in IR absorbance corresponds to the adsorption/desorption of anions ( $\text{ClO}_4^-$ ) on the surface of ML MoS<sub>2</sub> in HClO<sub>4</sub> electrolyte with respect to the reference spectrum at  $V_{EC} = 0$  V.<sup>28,29</sup> At  $V_{EC} = 0.3$  V vs RHE, the positive IR absorption signal indicates that more  $\text{ClO}_4^-$  anions adsorbed on the ML-MoS<sub>2</sub> surface because the positive bias potential is increased with respect to the reference bias of 0 V vs RHE. By contrast, a negative IR absorption signal at  $V_{EC} = -0.3$  V vs RHE is observed because the negatively charged  $\text{ClO}_4^-$  ions are repelled and fewer  $\text{ClO}_4^-$  ions are adsorbed onto the ML-MoS<sub>2</sub> surface as a negative bias is applied. Meanwhile, the positively charged  $\text{H}^+$  ions are also attracted and adsorbed onto

the surface of ML MoS<sub>2</sub>. Figure 3b and c schematically show the adsorption and desorption of negatively charged ClO<sub>4</sub><sup>-</sup> ions and positively charged H<sup>+</sup> ions onto the ML-MoS<sub>2</sub> surface for different applied bias potentials during the HER. The accumulated electrolyte ions on the ML-MoS<sub>2</sub> surface may form the nanometer-scale ECDL. To counter the formation of the ECDL at this interface, the carrier density or carrier type on the surface of the ML-MoS<sub>2</sub> catalyst is modulated due to the effect of electrolyte gating, similar to those observed in the gate-controlled MoS<sub>2</sub> FET devices.<sup>26</sup>

To further monitor the variation in the carrier type and density of MoS<sub>2</sub> under electrolyte gating during the HER, *in situ* Raman spectroscopy measurements on the electrochemical device were performed as shown in Figure 3d. Here, an immersion objective lens with an anticorrosive coating was used and directly immersed into the cell to collect the *in situ* Raman spectral signals. The peak positions and the line widths for the out-of-plane Raman A<sub>1g</sub> mode of MoS<sub>2</sub> have been reported to be sensitive to the variation in the electron concentrations for a gated MoS<sub>2</sub> FET<sup>26,30</sup> through strain,<sup>31,32</sup> which could be varied by tuning the charge doping via the substrates or interfaces.<sup>33–35</sup> The softening of the A<sub>1g</sub> modes in Raman spectra corresponds to an increase in electron doping concentrations when the electrochemical potential decreases from V<sub>EC</sub> = 0.3 to 0 V and -0.3 V vs RHE during the HER. The increased line width for the A<sub>1g</sub> mode in the Raman spectrum at V<sub>EC</sub> = -0.3 V vs RHE compared to that at V<sub>EC</sub> = 0 V vs RHE indicates a further increased electron doping concentration on the MoS<sub>2</sub> surface.<sup>26</sup> The adsorption of positively charged H<sup>+</sup> ions onto the ML-MoS<sub>2</sub> surface causes n-doping and an increased electron concentration at the HER-on state (V<sub>EC</sub> = -0.3 V vs RHE), while the adsorption of negatively charged ClO<sub>4</sub><sup>-</sup> ions on the ML-MoS<sub>2</sub> surface causes p-doping and a decreased electron concentration at the HER-off state (V<sub>EC</sub> = 0.3 V vs RHE) as shown in Figure 3b and c. Similar results cannot be observed in a ML-MoS<sub>2</sub> electrochemical device with DI water.

Because the as-grown CVD MoS<sub>2</sub> typically exhibits n-doping due to the inherent S-vacancy,<sup>9</sup> the accumulation of negatively charged ClO<sub>4</sub><sup>-</sup> ions on the ML-MoS<sub>2</sub> surface due to a positive V<sub>EC</sub> may suppress the formation of trions and enhance the formation of excitons, exhibiting the “intrinsic MoS<sub>2</sub>” behavior. As a result, the  $\Delta T/T$  curves as shown above exhibit the predominant optical signatures of excitons with a large percentage of the slow-component A<sub>2</sub> at the HER-off state. By contrast, the accumulation of positively charged H<sup>+</sup> ions onto the ML-MoS<sub>2</sub> surface at a negative V<sub>EC</sub> results in an increased electron concentration within MoS<sub>2</sub>, exhibiting the “strong n-doped MoS<sub>2</sub>” behavior (see Figure 3c). The  $\Delta T/T$  curves exhibit the predominant optical signatures of trions with a large percentage of fast-component A<sub>1</sub> at the HER-on state. Accordingly, the accumulation of electrolyte ions ClO<sub>4</sub><sup>-</sup> or hydrogen ions on the ML-MoS<sub>2</sub> surface during electrocatalytic reactions by applying a positive or a negative V<sub>EC</sub> may modulate the carrier concentrations of MoS<sub>2</sub> catalysts. Such a “self-gating” phenomenon is particularly important for the ultrathin semiconductor catalysts, such as 2D TMDs.<sup>14</sup> By employing the above operando probing techniques of the TR-LCM combined with *in situ* IR and *in situ* Raman spectroscopies, the interplay between exciton/trion relaxation dynamics and electrocatalytic activity for the ML MoS<sub>2</sub> affected by electrolyte gating during the HER process can be unveiled.

**Ultrafast Time Evolution of Trion/Exciton Distributions on ML MoS<sub>2</sub> in a Liquid Electrolyte.** The optical signatures of excitons and trions may act as sensitive descriptors to monitor the local surface charge density for MoS<sub>2</sub> under electrolyte gating. Therefore, we are able to spatially visualize the electrocatalytic activity of ML MoS<sub>2</sub> affected by electrolyte gating during the HER through performing the mapping of the individual fast and slow components of ( $\tau_1$ , A<sub>1</sub>) and ( $\tau_2$ , A<sub>2</sub>) across the entire ML MoS<sub>2</sub> flake. Figure 4a and b show the evolution of the mapping images of trions (fast component, red) and excitons (slow components, blue) on ML MoS<sub>2</sub> for V<sub>EC</sub> = 0.3, 0, and -0.3 V vs RHE, respectively. The above result suggests the fast-component region resulting from trions (red) represents the local charge environment of “n-doped” MoS<sub>2</sub> which is more conductive because there is a higher electron concentration. The slow-component region resulting from excitons represents the local charge environment of “intrinsic” MoS<sub>2</sub> (blue) which is insulated or less conductive because there is a lower electron concentration. At V<sub>EC</sub> = 0.3 V, the entire MoS<sub>2</sub> flake is predominated by the slow component of excitons (or intrinsic MoS<sub>2</sub>). The adsorption of negatively charged ClO<sub>4</sub><sup>-</sup> ions onto the MoS<sub>2</sub> surface due to a positive V<sub>EC</sub> results in a decreased electron concentration, so that the surface of MoS<sub>2</sub> becomes less conductive and there is no electrocatalytic reaction. This shows the HER-off state. Although a small portion of the fast components of trions (or n-doped MoS<sub>2</sub>) are distributed within the MoS<sub>2</sub> flake, they do not form an effective charge transport pathway. As V<sub>EC</sub> decreases to 0 V vs RHE, an increased number of the fast component of trions and a decreased number of the slow components of excitons are observed. As V<sub>EC</sub> further decreases to -0.3 V vs RHE, the entire MoS<sub>2</sub> is predominated by the fast components of trions (or n-doped MoS<sub>2</sub>). The adsorption of positively charged H<sup>+</sup> ions onto the MoS<sub>2</sub> surface by applying a negative V<sub>EC</sub> increases the electron concentrations of MoS<sub>2</sub> due to the electrolyte-gating effect, so that the entire MoS<sub>2</sub> flake becomes conductive and active for electrocatalytic reactions. This is the HER-on state. The result is consistent with the recent observation of enhanced surface conduction on a 2D TMD catalyst surface due to the self-gating effect using the *in situ* electronic/electrochemical measurements.<sup>14</sup>

In contrast to the electronic measurement technique, our optical measurement technique for this study gives spatially resolved information about the catalytic activity of ML MoS<sub>2</sub> during the HER affected by the electrolyte ions. For example, it can be seen that at the HER-on state with V<sub>EC</sub> = -0.3 V, some areas in the MoS<sub>2</sub> flake in Figure 4a exhibit a higher percentage of the fast components of trions (dark red region) than other regions (light red region). The inhomogeneous distribution of the fast components of trions on the MoS<sub>2</sub> surface affected by electrolyte gating may be related to the intrinsic nature of 2D TMD semiconductor catalysts which usually consist of a mixture of “active” and “inert” sites,<sup>16</sup> which is, respectively, due to the appearance and disappearance of defects (e.g., S-vacancy) and can be indicated by the trion dynamics. Figure 4c shows the time evolution of the mapping images of the slow components for excitons at V<sub>EC</sub> = 0.3 V and the fast components for trions at V<sub>EC</sub> = -0.3 V. The mapping image of the slow components for excitons can still be seen at a time scale longer than 20 ps; by contrast, the mapping image of the fast components for trions is nearly vanished at a time scale of 4 ps especially within the green dashed ellipses close to the

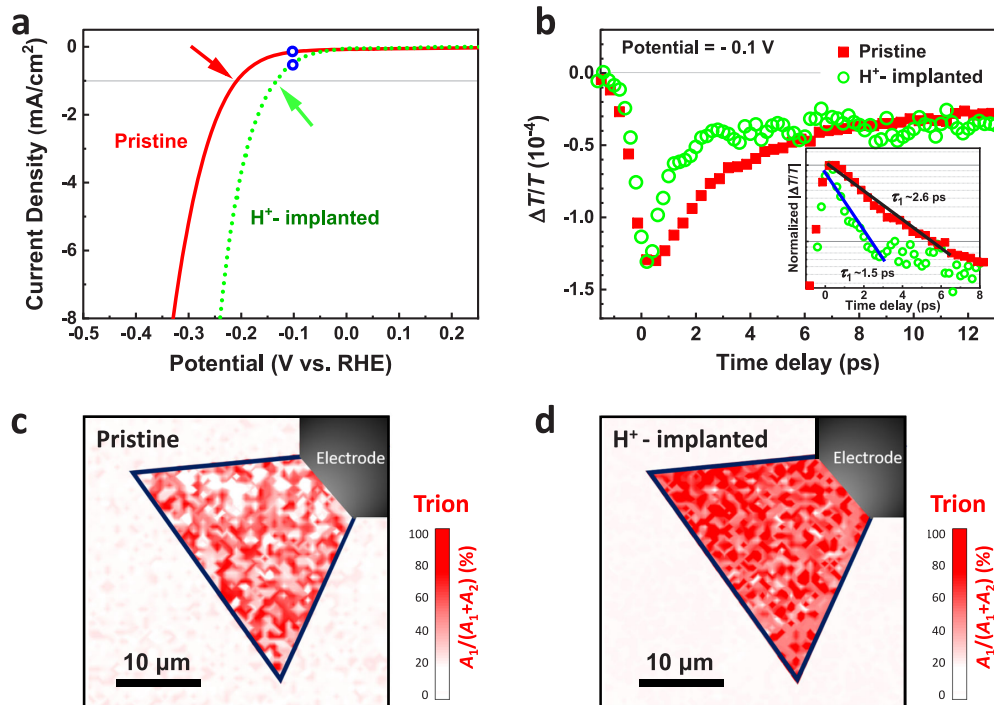


**Figure 5.** HER performance and ultrafast carrier dynamics for pristine and H<sup>+</sup>-implanted ML MoS<sub>2</sub>. (a) Current density as a function of potentials for pristine and H<sup>+</sup>-implanted ML MoS<sub>2</sub> in HClO<sub>4</sub> electrolyte. The arrows mark the onset potential vs RHE (current density = −1 mA/cm<sup>2</sup>) for the HER. (b) Ultrafast carrier dynamics for pristine (extracted from Figure 2c) and H<sup>+</sup>-implanted ML MoS<sub>2</sub> with a potential of  $V_{EC} = -0.1$  V vs RHE. Inset: Normalized  $|\Delta T/T|$  of part b plotted in semilogarithmic scale. Solid lines are the linear fitting with the relaxation time constant  $\tau_1$ . (c and d) 2D mappings of the amplitude ratio for the fast ( $A_1$ ) relaxation component to the total amplitude ( $A_1 + A_2$ ) of  $\Delta T/T$  in part b at zero time delay ( $t = 0$  ps) using a TR-LCM.

edge of a MoS<sub>2</sub> single flake in Figure 4c. The carrier dynamics of ML MoS<sub>2</sub> can be varied from slow relaxed excitons to fast relaxed trions by changing the  $V_{EC}$  from 0.3 V (HER-off state) to −0.3 V (HER-on state). According to the discussion in section S3 of the Supporting Information, additionally, the hydrogen evolution reaction is more active and efficient in the edge region (the region marked by a green ellipse close to the edge of a MoS<sub>2</sub> single flake in Figure 4a), which is consistent with the results of electrocatalytic activity measurements on the MoS<sub>2</sub> catalyst by STM study.<sup>16</sup> Based on the distinct carrier dynamics of excitons and trions of MoS<sub>2</sub>, our TR-LCM technique allows in situ monitoring of the local charge environment at the atomic layer/liquid electrolyte interfaces and the corresponding catalytic activity of 2D TMDs affected by electrolyte gating during electrochemical reactions.

**HER Performance and Ultrafast Carrier Dynamics for Pristine and H<sup>+</sup>-Implanted ML MoS<sub>2</sub>.** It has been demonstrated that the electrocatalytic HER activity of pristine MoS<sub>2</sub> can be further enhanced by introducing more active sites through defect engineering using plasma exposure or annealing treatment.<sup>36</sup> The catalytic activity of ML MoS<sub>2</sub> is enhanced by defect engineering because S-vacancies are created, which increases hydrogen adsorption and the density of active sites.<sup>7,11</sup> Here, we have employed the post-treatment of H<sup>+</sup> implantation to perform defect engineering on ML MoS<sub>2</sub>. Figure 5a shows the HER performance for the ML-MoS<sub>2</sub> catalysts without and with the post-treatment of H<sup>+</sup> implantation. The ML-MoS<sub>2</sub> catalyst with the post-treatment of H<sup>+</sup> implantation exhibits an improved HER performance compared to the as-grown pristine ML MoS<sub>2</sub>, yielding an onset of −0.13 V (H<sup>+</sup>-implantation) and −0.21 V (pristine) at the

current density of −1 mA/cm<sup>2</sup>. Additionally, the in situ PL/Raman spectra of H<sup>+</sup>-implanted ML MoS<sub>2</sub> are similar to those of the pristine case in Figure 3d and Figure S1 of the Supporting Information.

Figure 5b shows the corresponding bias-dependent  $\Delta T/T$  spectra for ML-MoS<sub>2</sub> electrochemical devices without and with the post-treatment at  $V_{EC} = -0.1$  V vs RHE during the HER process. The ML MoS<sub>2</sub> with the post-treatment exhibits a much faster pump–probe relaxation curve with a higher percentage of fast components for trions (~89%) compared to that of the as-grown pristine MoS<sub>2</sub> sample with a fast component (~57%) (see the inset of Figure 5b) as they were operated at the same conditions for the electrochemical reaction. Figure 5c and d show the 2D mapping images of fast components for trions on the surface of post-treated ML MoS<sub>2</sub> than on the surface of pristine ML MoS<sub>2</sub>. Accordingly, the enhanced electrocatalytic activity of ML MoS<sub>2</sub> by creating more active sites through the post-treatment of H<sup>+</sup> implantation can be spatially visualized by our TR-LCM technique.

## CONCLUSION

In summary, we have demonstrated that the distinct carrier dynamics of excitons and trions on the MoS<sub>2</sub> surface can act as sensitive descriptors to monitor the local electrocatalytic activity affected by electrolyte gating during the HER. The operando probing technique of the TR-LCM revealed the

interplay between exciton/trion dynamics and electrocatalytic activity for ML MoS<sub>2</sub> affected by electrolyte gating during the HER process. The adsorption of positively charged H<sup>+</sup> ions onto the MoS<sub>2</sub> surface by applying a negative  $V_{EC}$  also modulates the carrier concentrations of MoS<sub>2</sub> due to the electrolyte-gating (or self-gating) effect, so that the entire MoS<sub>2</sub> flake becomes conductive and active for electrocatalytic reactions. This is directly visualized from the evolution of mapping images of the distributions of excitons and trions on the MoS<sub>2</sub> surface during the HER process. The operando probing technique of the TR-LCM provides an excellent platform to explore local carrier behaviors at the atomic layer/liquid electrolyte interfaces during electrocatalytic reaction for 2D TMDs.

## METHODS

**Sample Preparation.** Figure 1 shows a HER device fabricated with a single 2D atomic monolayer MoS<sub>2</sub> flake. The MoS<sub>2</sub> flakes were transferred to a sapphire substrate. As shown in Figure 1c, one Au/Cr electrode was deposited on one corner of a single 2D atomic layer MoS<sub>2</sub> flake to provide the bias potential for the HER. In order to protect the electrode and to define the HER area, the photoresist was coated on the Au/Cr electrode and sapphire substrate. The electrolyte HClO<sub>4</sub> (1 M) filled the area for the HER, which was confined by an O-ring on the surface of the photoresist and a piece of glass. The working electrode (WE) was in contact with the Au/Cr metallic pad. The counter electrode (CE) and reference electrode (RE) were dipped in the electrolyte HClO<sub>4</sub> through a hole between the glass and the O-ring.

**Time-Resolved Liquid Cell Microscope (TR-LCM).** In this study, the in situ ultrafast carrier dynamics in MoS<sub>2</sub> during the HER was studied using 400 nm pump and 800 nm probe spectroscopy as shown in Figure 1a. The light source was a Ti:sapphire laser (Femtosource scientific XL300, Femtolaser) with a central wavelength of 800 ( $\pm 16$ ) nm, a repetition rate of 5.2 MHz, and a pulse width of 100 fs. After the Ti:sapphire laser, the laser pulse was split into one pump pulse and one probe pulse by a beam splitter (BS). For the pump pulses, a  $\beta$ -BaB<sub>2</sub>O<sub>4</sub> (BBO) nonlinear crystal was used to convert the wavelength from 800 to 400 nm after an acousto-optic modulator (AOM),<sup>37</sup> which modulated the pump beam for the reference frequency of a lock-in amplifier.<sup>38</sup> A delay stage was used to adjust the optical path length of pump pulses and further control the time delay between pump and probe pulses. The polarizations of pump and probe pulses were set to be perpendicular to eliminate the coherent spike around zero time delay.<sup>39</sup> Finally, the pump pulses and probe pulses were combined by a dichroic beam splitter (DBS) and collimated to a microscope system.

For the measurements of spatially resolved ultrafast carrier dynamics, a laser scanning microscope combined with the above pump–probe system was used to map the MoS<sub>2</sub> during the HER. The pump and probe pulses were focused on the MoS<sub>2</sub> using an objective lens after a galvo mirror (GM), which allowed spatial mapping. The transmitted pulses were collected by the other objective lens, and only the probe pulse was sent to the photodiode (PD) through a filter. The position-dependent transient transmittance changes ( $\Delta T/T$ ) were measured by controlling the time delay between pump and probe pulses. In this study, the spatial resolution was about 2  $\mu\text{m}$  and the typical pump and probe fluences were 200 and 10  $\mu\text{J}/\text{cm}^2$ , respectively.

**In Situ PL and Raman.** The in situ PL and Raman spectroscopy measurements were carried out in our homemade system. The light source was the frequency-doubled Nd:YAG laser with a wavelength of 532 nm. The MoS<sub>2</sub> samples with working electrode (WE), Pt counter electrode (CE), and Ag/AgCl (3 M KCl) reference electrode (RE) were placed into a customized Teflon cell filled with the HClO<sub>4</sub> electrolyte. An immersion objective lens (40 $\times$ ) with an antireflective coating was used and directly immersed into the cell. The applied potential was given by the 760D CH Instruments potentiostat. All of

the spectra were acquired through the spectrometer (Kymera 193i-B2, Andor) with the grating of 1200 l/mm and the low-noise CCD (iVac316, Andor) which was cooled down to  $-50^\circ\text{C}$ .

**Electrochemical FTIR Spectroscopy.** In situ FTIR spectroscopy was performed in a home-built reflection accessory with internal reflection configuration using a Thermo Nicolet 6700 FTIR spectrometer that was equipped with a HgCdTe (MCT) detector.<sup>40</sup> All spectra were acquired with a spectral resolution of 4  $\text{cm}^{-1}$ . The acquisition time for each spectrum was 10 s. The spectroelectrochemical measurements were performed using a 760D CH Instruments potentiostat. A Pt mesh and RHE electrode were respectively used as counter and reference electrodes. The electrolyte for all spectro-electrochemical measurements was HClO<sub>4</sub>. In the present study, the reference condition is the ML-MoS<sub>2</sub> material in 1 M HClO<sub>4</sub> electrolyte at 0 V. Compared to the reference condition, the IR peaks with positive absorbance suggest that the species are formed or the amount of the species increases on the surface. In contrast, the IR peaks with negative absorbance suggest that the amount of the species is reduced.

**H<sup>+</sup>-Implanted MoS<sub>2</sub> HER Devices.** In this study, atomic defects were created on the pristine MoS<sub>2</sub> to improve its HER efficiency. The H<sup>+</sup>-implanted MoS<sub>2</sub> HER devices were fabricated using H<sup>+</sup> ion implantation with a medium current ion implanter (Ulvac IMX-3500). Ionized H<sup>+</sup> ions were selected through a mass spectrometer and then accelerated to 20 keV. The device was implanted at a dose of  $1 \times 10^{15}$  ions/ $\text{cm}^2$  with a stable low current to avoid local heating during ion bombardments.

## ASSOCIATED CONTENT

### Supporting Information

The Supporting Information is available free of charge at <https://pubs.acs.org/doi/10.1021/acsnano.1c10380>.

In situ PL spectra of ML MoS<sub>2</sub> in HClO<sub>4</sub> with different potentials; potential-dependent ultrafast carrier dynamics of ML MoS<sub>2</sub> in HClO<sub>4</sub>;  $\Delta T/T$  in the basal and edge regions of ML MoS<sub>2</sub> in HClO<sub>4</sub>; pump fluence-dependent  $\Delta T/T$  of ML MoS<sub>2</sub> in HClO<sub>4</sub>; and in situ PL and Raman spectra of ML MoS<sub>2</sub> in DI water with different potentials (PDF)

## AUTHOR INFORMATION

### Corresponding Authors

**Chun-Wei Chen** — Department of Materials Science and Engineering, National Taiwan University, Taipei 10617, Taiwan; Center of Atomic Initiative for New Materials (AI-MAT), National Taiwan University, Taipei 10617, Taiwan; Taiwan Consortium of Emergent Crystalline Materials (TCECM), Ministry of Science and Technology, Taipei 10622, Taiwan;  [orcid.org/0000-0003-3096-249X](https://orcid.org/0000-0003-3096-249X); Email: [chunwei@ntu.edu.tw](mailto:chunwei@ntu.edu.tw)

**Chih-Wei Luo** — Department of Electrophysics and Institute of Physics and Center for Emergent Functional Matter Science, National Yang Ming Chiao Tung University, Hsinchu 30010, Taiwan; Taiwan Consortium of Emergent Crystalline Materials (TCECM), Ministry of Science and Technology, Taipei 10622, Taiwan; National Synchrotron Radiation Research Center, Hsinchu 30076, Taiwan;  [orcid.org/0000-0002-6453-7435](https://orcid.org/0000-0002-6453-7435); Email: [cwluoep@nycu.edu.tw](mailto:cwluoep@nycu.edu.tw)

### Authors

**Fu-He Hsiao** — Department of Electrophysics, National Yang Ming Chiao Tung University, Hsinchu 30010, Taiwan

**Cheng-Chu Chung** — Department of Materials Science and Engineering, National Taiwan University, Taipei 10617, Taiwan

Chun-Hao Chiang – Department of Materials Science and Engineering, National Taiwan University, Taipei 10617, Taiwan

Wei-Neng Feng – Department of Electrophysics, National Yang Ming Chiao Tung University, Hsinchu 30010, Taiwan

Wen-Yen Tzeng – Department of Electrophysics, National Yang Ming Chiao Tung University, Hsinchu 30010, Taiwan

Hung-Min Lin – Department of Materials Science and Engineering, National Taiwan University, Taipei 10617, Taiwan

Chien-Ming Tu – Department of Electrophysics, National Yang Ming Chiao Tung University, Hsinchu 30010, Taiwan

Heng-Liang Wu – Center for Condensed Matter Sciences and Center of Atomic Initiative for New Materials (AI-MAT), National Taiwan University, Taipei 10617, Taiwan;

 [orcid.org/0000-0003-1250-9851](https://orcid.org/0000-0003-1250-9851)

Yu-Han Wang – Department of Physics, National Central University, Taoyuan 32001, Taiwan; Molecular Science and Technology Program, Taiwan International Graduate Program, Institute of Atomic and Molecular Science, Academia Sinica, Taipei 10617, Taiwan

Wei-Yen Woon – Department of Physics, National Central University, Taoyuan 32001, Taiwan; Molecular Science and Technology Program, Taiwan International Graduate Program, Institute of Atomic and Molecular Science, Academia Sinica, Taipei 10617, Taiwan;  [orcid.org/0000-0001-7299-9122](https://orcid.org/0000-0001-7299-9122)

Hsiao-Chien Chen – Center for Reliability Science and Technologies, Chang Gung University, Taoyuan 33302, Taiwan; Kidney Research Center, Department of Nephrology, Chang Gung Memorial Hospital, Linkou, Taoyuan 333, Taiwan

Ching-Hsiang Chen – Sustainable Energy Development Center, National Taiwan University of Science and Technology, Taipei 106335, Taiwan

Chao-Yuan Lo – Center for Condensed Matter Sciences and Center of Atomic Initiative for New Materials (AI-MAT), National Taiwan University, Taipei 10617, Taiwan

Man-Hong Lai – Center for Condensed Matter Sciences, National Taiwan University, Taipei 10617, Taiwan

Yu-Ming Chang – Center for Condensed Matter Sciences and Center of Atomic Initiative for New Materials (AI-MAT), National Taiwan University, Taipei 10617, Taiwan

Li-Syuan Lu – Department of Electrophysics, National Yang Ming Chiao Tung University, Hsinchu 30010, Taiwan

Wen-Hao Chang – Department of Electrophysics, National Yang Ming Chiao Tung University, Hsinchu 30010, Taiwan; Taiwan Consortium of Emergent Crystalline Materials (TCECM), Ministry of Science and Technology, Taipei 10622, Taiwan;  [orcid.org/0000-0003-4880-6006](https://orcid.org/0000-0003-4880-6006)

Complete contact information is available at:

<https://pubs.acs.org/10.1021/acsnano.1c10380>

## Author Contributions

<sup>†</sup>F.H.H., C.C.C., and C.H.C. contributed equally to this work.

## Author Contributions

C.W.L. and C.W.C. proposed the project. F.H.H., W.N.F., W.Y.T., C.M.T., C.Y.L., M.H.L. and Y.M.C. developed the spatially resolved pump–probe experimental setup and collected the data. C.C.C., Y.H.W., W.Y.W., L.S.L. and W.H.C. prepared the samples. H.L.W. performed the measurements of IR absorbance spectra. The manuscript was written

by C.W.L. and C.W.C. All authors edited and approved the final manuscript.

## Notes

The authors declare no competing financial interest.

## ACKNOWLEDGMENTS

This work was supported by the Ministry of Science and Technology of the Republic of China, Taiwan (Grant Nos. 109-2112-M-009-020-MY3, 109-2124-M-009-003-MY3, and 109-2628-M-008-004-MY3) and the Center for Emergent Functional Matter Science of National Yang Ming Chiao Tung University from The Featured Areas Research Center Program and the Research Team of Photonic Technologies and Intelligent Systems at NYCU within the framework of the Higher Education Sprout Project by the Ministry of Education (MOE) in Taiwan.

## REFERENCES

- (1) Turner, J. A. Sustainable Hydrogen Production. *Science* **2004**, *305*, 972–974.
- (2) Greeley, J.; Jaramillo, T. F.; Bonde, J.; Chorkendorff, I.; Nørskov, J. K. Computational High-Throughput Screening of Electrocatalytic Materials for Hydrogen Evolution. *Nat. Mater.* **2006**, *5*, 909–913.
- (3) Nørskov, J. K.; Bligaard, T.; Logadottir, A.; Kitchin, J. R.; Chen, J. G.; Pandelov, S.; Stimming, U. Trends in the Exchange Current for Hydrogen Evolution. *J. Electrochem. Soc.* **2005**, *152*, J23–J26.
- (4) Wang, Q. H.; Kalantar-Zadeh, K.; Kis, A.; Coleman, J. N.; Strano, M. S. Electronics and Optoelectronics of Two-Dimensional Transition Metal Dichalcogenides. *Nat. Nanotechnol.* **2012**, *7*, 699–712.
- (5) Xu, M.; Liang, T.; Shi, M.; Chen, H. Graphene-Like Two-Dimensional Materials. *Chem. Rev.* **2013**, *113*, 3766–3798.
- (6) Chhowalla, M.; Shin, H. S.; Eda, G.; Li, L.-J.; Loh, K. P.; Zhang, H. The Chemistry of Two-Dimensional Layered Transition Metal Dichalcogenide Nanosheets. *Nat. Chem.* **2013**, *5*, 263–275.
- (7) Hinnemann, B.; Moses, P. G.; Bonde, J.; Jørgensen, K. P.; Nielsen, J. H.; Horch, S.; Chorkendorff, I.; Nørskov, J. K. Biomimetic Hydrogen Evolution: MoS<sub>2</sub>Nanoparticles as Catalyst for Hydrogen Evolution. *J. Am. Chem. Soc.* **2005**, *127*, 5308–5309.
- (8) Voiry, D.; Salehi, M.; Silva, R.; Fujita, T.; Chen, M.; Asefa, T.; Shenoy, V. B.; Eda, G.; Chhowalla, M. Conducting MoS<sub>2</sub>Nanosheets as Catalysts for Hydrogen Evolution Reaction. *Nano Lett.* **2013**, *13*, 6222–6227.
- (9) Li, H.; Tsai, C.; Koh, A. L.; Cai, L.; Contryman, A. W.; Fragapane, A. H.; Zhao, J.; Han, H. S.; Manoharan, H. C.; Abild-Pedersen, F.; Nørskov, J. K.; Zheng, X. Activating and Optimizing MoS<sub>2</sub>Basal Planes for Hydrogen Evolution through the Formation of Strained Sulphur Vacancies. *Nat. Mater.* **2016**, *15*, 48–53.
- (10) Xie, J.; Zhang, H.; Li, S.; Wang, R.; Sun, X.; Zhou, M.; Zhou, J.; Lou, X. W.; Xie, Y. Defect-Rich MoS<sub>2</sub>Ultrathin Nanosheets with Additional Active Edge Sites for Enhanced Electrocatalytic HydrogenEvolution. *Adv. Mater.* **2013**, *25*, 5807–5813.
- (11) Xie, J.; Zhang, J.; Li, S.; Grote, F.; Zhang, X.; Zhang, H.; Wang, R.; Lei, Y.; Pan, B.; Xie, Y. Controllable Disorder Engineering in Oxygen-Incorporated MoS<sub>2</sub>Ultrathin Nanosheets for Efficient Hydrogen Evolution. *J. Am. Chem. Soc.* **2013**, *135*, 17881–17888.
- (12) Gao, G.; Jiao, Y.; Ma, F.; Jiao, Y.; Waclawik, E.; Du, A. Charge Mediated Semiconductor-to-Metallic Phase Transition in Molybdenum Disulfide Monolayer and Hydrogen Evolution Reaction in New 1T' Phase. *J. Phys. Chem. C* **2015**, *119*, 13124–13128.
- (13) Yin, Y.; Han, J.; Zhang, Y.; Zhang, X.; Xu, P.; Yuan, Q.; Samad, L.; Wang, X.; Wang, Y.; Zhang, Z.; Zhang, P.; Cao, X.; Song, B.; Jin, S. Contributions of Phase, Sulfur Vacancies, and Edges to the Hydrogen Evolution Reaction Catalytic Activity of Porous Molybdenum Disulfide Nanosheets. *J. Am. Chem. Soc.* **2016**, *138*, 7965–7972.
- (14) He, Y.; He, Q.; Wang, L.; Zhu, C.; Golani, P.; Handoko, A. D.; Yu, X.; Gao, C.; Ding, M.; Wang, X.; Liu, F.; Zeng, Q.; Yu, P.; Guo,

- S.; Yakobson, B. I.; Wang, L.; Seh, Z. W.; Zhang, Z.; Wu, M.; Wang, Q. J.; Zhang, H.; Liu, Z. Self-Gating in Semiconductor Electrocatalysis. *Nat. Mater.* **2019**, *18*, 1098–1104.
- (15) Franklin, A. D. *Electrocatalysis on Non-Metallic Surfaces*; U.S. Department of Commerce: Washington, D.C., 1976; pp 1–358.
- (16) Jaramillo, T. F.; Jorgensen, K. P.; Bonde, J.; Nielsen, J. H.; Horch, S.; Chorkendorff, I. Identification of Active Edge Sites for Electrochemical H<sub>2</sub> Evolution from MoS<sub>2</sub> Nanocatalysts. *Science* **2007**, *317*, 100–102.
- (17) Mak, K. F.; He, K.; Lee, C.; Lee, G. H.; Hone, J.; Heinz, T. F.; Shan, J. Tightly Bound Trions in Monolayer MoS<sub>2</sub>. *Nat. Mater.* **2013**, *12*, 207–211.
- (18) Stébé, B.; Ainane, A. Ground State Energy and Optical Absorption of Excitonic Trions in Two Dimensional Semiconductors. *Superlattice. Microst.* **1989**, *5*, 545–548.
- (19) Hawrylak, P. Optical Properties of A Two-Dimensional Electron Gas: Evolution of Spectra from Excitons to Fermi-Edge Singularities. *Phys. Rev. B* **1991**, *44*, 3821–3828.
- (20) Ogawa, T. Quantum States and Optical Responses of Low-Dimensional Electron-Hole Systems. *J. Phys.: Condens. Matter* **2004**, *16*, S3567–S3595.
- (21) Sun, D.; Rao, Y.; Reider, G. A.; Chen, G.; You, Y.; Brézin, L.; Harutyunyan, A. R.; Heinz, T. F. Observation of Rapid Exciton–Exciton Annihilation in Monolayer Molybdenum Disulfide. *Nano Lett.* **2014**, *14*, 5625–5629.
- (22) Goswami, T.; Rani, R.; Hazra, K. S.; Ghosh, H. N. Ultrafast Carrier Dynamics of the Exciton and Trion in MoS<sub>2</sub> Monolayers Followed by Dissociation Dynamics in Au@MoS<sub>2</sub> 2D Heterointerfaces. *J. Phys. Chem. Lett.* **2019**, *10*, 3057–3063.
- (23) Mouri, S.; Miyauchi, Y.; Matsuda, K. Tunable Photoluminescence of Monolayer MoS<sub>2</sub> via Chemical Doping. *Nano Lett.* **2013**, *13*, 5944–5948.
- (24) Ross, J. S.; Wu, S.; Yu, H.; Ghimire, N. J.; Jones, A. M.; Aivazian, G.; Yan, J.; Mandrus, D. G.; Xiao, D.; Yao, W.; Xu, X. Electrical Control of Neutral and Charged Excitons in A Monolayer Semiconductor. *Nat. Commun.* **2013**, *4*, 1474.
- (25) Zhang, Q.; Wang, W.; Zhang, J.; Zhu, X.; Zhang, Q.; Zhang, Y.; Ren, Z.; Song, S.; Wang, J.; Ying, Z.; Wang, R.; Qiu, X.; Peng, T.; Fu, L. Highly Efficient Photocatalytic Hydrogen Evolution by ReS<sub>2</sub> via A Two-Electron Catalytic Reaction. *Adv. Mater.* **2018**, *30*, 1707123.
- (26) Liu, X.; Li, B.; Li, X.; Harutyunyan, A. R.; Hone, J.; Esposito, D. V. The Critical Role of Electrolyte Gating on the Hydrogen Evolution Performance of Monolayer MoS<sub>2</sub>. *Nano Lett.* **2019**, *19*, 8118–8124.
- (27) H L, P.; Mondal, P.; Bid, A.; Basu, J. K. Electrical and Chemical Tuning of Exciton Lifetime in Monolayer MoS<sub>2</sub> for Field-Effect Transistors. *ACS Appl. Nano Mater.* **2020**, *3*, 641–647.
- (28) Ataka, K.; Yotsuyanagi, T.; Osawa, M. Potential-Dependent Reorientation of Water Molecules at An Electrode/electrolyte Interface Studied by Surface-Enhanced Infrared Absorption Spectroscopy. *J. Phys. Chem.* **1996**, *100*, 10664–10672.
- (29) Garcia-Araez, N.; Rodriguez, P.; Bakker, H. J.; Koper, M. T. M. Effect of the Surface Structure of Gold Electrodes on the Coadsorption of Water and Anions. *J. Phys. Chem. C* **2012**, *116*, 4786–4792.
- (30) Carroll, G. M.; Zhang, H.; Dunklin, J. R.; Miller, E. M.; Neale, N. R.; van de Lagemaat, J. Unique Interfacial Thermodynamics of Few-Layer 2D MoS<sub>2</sub> for (Photo)electrochemical Catalysis. *Energy Environ. Sci.* **2019**, *12*, 1648–1656.
- (31) Rao, R.; Islam, A. E.; Singh, S.; Berry, R.; Kawakami, R. K.; Maruyama, B.; Katoch, J. Spectroscopic Evaluation of Charge-Transfer Doping and Strain in Graphene/MoS<sub>2</sub> Heterostructures. *Phys. Rev. B* **2019**, *99*, 195401.
- (32) Chae, W. H.; Cain, J. D.; Hanson, E. D.; Murthy, A. A.; Dravid, V. P. Substrate-Induced Strain and Charge Doping in CVD-Grown Monolayer MoS<sub>2</sub>. *Appl. Phys. Lett.* **2017**, *111*, 143106.
- (33) Zhang, H.; Dunklin, J. R.; Reid, O. G.; Yun, S. J.; Nanayakkara, S. U.; Lee, Y. H.; Blackburn, J. L.; Miller, E. M. Disentangling Oxygen and Water Vapor Effects on Optoelectronic Properties of Monolayer Tungsten Disulfide. *Nanoscale* **2020**, *12*, 8344–8354.
- (34) Rosa, C. J. L.; Phillipson, R.; Teyssandier, J.; Adisoejoso, J.; Balaji, Y.; Huyghebaert, C.; Radu, I.; Heyns, M.; Feyter, S. D.; Gendt, S. D. Molecular Doping of MoS<sub>2</sub> Transistors by Self-Assembled Oleylamine Networks. *Appl. Phys. Lett.* **2016**, *109*, 253112.
- (35) Kiriya, D.; Tosun, M.; Zhao, P.; Kang, J. S.; Javey, A. Air-Stable Surface Charge Transfer Doping of MoS<sub>2</sub> by Benzyl Viologen. *J. Am. Chem. Soc.* **2014**, *136*, 7853–7856.
- (36) Ye, G.; Gong, Y.; Lin, J.; Li, B.; He, Y.; Pantelides, S. T.; Zhou, W.; Vajtai, R.; Ajayan, P. M. Defects Engineered Monolayer MoS<sub>2</sub> for Improved Hydrogen Evolution Reaction. *Nano Lett.* **2016**, *16*, 1097–1103.
- (37) Wu, K. H.; Chen, H.-J.; Chen, Y. T.; Hsieh, C. C.; Luo, C. W.; Uen, T. M.; Juang, J. Y.; Lin, J.-Y.; Kobayashi, T.; Gospodinov, M. Marked Enhancement of Néel Temperature in Strained YMnO<sub>3</sub> Thin Films Probed by Femtosecond Spectroscopy. *EPL* **2011**, *94*, 27006.
- (38) Luo, C. W.; Wang, Y. T.; Chen, F. W.; Shih, H. C.; Kobayashi, T. Eliminate Coherence Spike in Reflection-Type Pump-Probe Measurements. *Opt. Express* **2009**, *17*, 11321–11327.
- (39) Luo, C. W.; Wang, Y. T.; Yabushita, A.; Kobayashi, T. Ultrabroadband Time-Resolved Spectroscopy in Novel Types of Condensed Matter. *Optica* **2016**, *3*, 82–92.
- (40) Chou, T.-C.; Chang, C.-C.; Yu, H.-L.; Yu, W.-Y.; Dong, C.-L.; Velasco-Vélez, J.-J.; Chuang, C.-H.; Chen, L.-C.; Lee, J.-F.; Chen, J.-M.; Wu, H.-L. Controlling the Oxidation State of the Cu Electrode and Reaction Intermediates for Electrochemical CO<sub>2</sub> Reduction to Ethylene. *J. Am. Chem. Soc.* **2020**, *142*, 2857–2867.

## □ Recommended by ACS

### Electron Tunneling at Electrocatalytic Interfaces

Mohammad R. Nouri, Vitaly Alexandrov, et al.

MARCH 27, 2023

THE JOURNAL OF PHYSICAL CHEMISTRY C

READ ▶

### Nanoscale Cathodoluminescence and Conductive Mode Scanning Electron Microscopy of van der Waals Heterostructures

Hugh Ramsden, Manish Chhowalla, et al.

JUNE 15, 2023

ACS NANO

READ ▶

### Heterogeneity between and within Single Hematite Nanorods as Electrocatalysts for Oxygen Evolution Reaction

Mingyang Li, Hang Ren, et al.

MARCH 17, 2022

JOURNAL OF THE AMERICAN CHEMICAL SOCIETY

READ ▶

### Bifunctional Monolayer WSe<sub>2</sub>/Graphene Self-Stitching Heterojunction Microreactors for Efficient Overall Water Splitting in Neutral Medium

Chun-Hao Chiang, Chun-Wei Chen, et al.

OCTOBER 28, 2022

ACS NANO

READ ▶

Get More Suggestions >